

1 **Permafrost, active layer, and meteorological data (2010–**
2 **2020) at the Mahan Mountain relict permafrost site of**
3 **Northeastern Qinghai-Tibet Plateau**

4
5 Tonghua Wu^{1,2*}, Changwei Xie¹, Xiaofan Zhu¹, Jie Chen¹, Wu Wang¹, Ren Li¹, Amin
6 Wen¹, Dong Wang¹, Peiqing Lou¹, Chengpeng Shang¹, Yune La¹, Xianhua Wei¹, Xin Ma¹,
7 Yongping Qiao¹, Xiaodong Wu¹, Qiangqiang Pang¹, Guojie Hu¹

8 ¹ Cryosphere Research Station on the Qinghai-Tibet Plateau, State Key Laboratory of
9 Cryospheric Science, Northwest Institute of Eco-Environment and Resource, Chinese
10 Academy of Sciences, Lanzhou, Gansu 730000, China

11 ² Southern Marine Science and Engineering Guangdong Laboratory (Guangzhou),
12 511458, China

13 *Correspondence: Tonghua Wu (thuawu@lzb.ac.cn)

14 **Abstract:** Relict permafrost presents an ideal opportunity to understand the impacts
15 of climatic warming on the ground thermal regime since it is characterized by a mean
16 annual ground temperature close to 0 °C and relatively thin permafrost. The long-term
17 and continuous observations of permafrost thermal state and climate background are
18 of great importance to reveal the links between the energy balance on hourly to annual
19 timescales, to evaluate the variations in permafrost thermal state over multiannual
20 periods and to validate the remote sensing dataset. We present 11 years of
21 meteorological and soil data from the Mahan Mountain relict permafrost site on the
22 northeast of the Qinghai-Tibet Plateau. The meteorological data comprise air and land
23 surface temperature, relative humidity, wind speed and direction, shortwave and
24 longwave downwards and upwards radiation, water vapor pressure, and precipitation
25 on a half-hour timescale. The active layer data include daily soil temperature and soil
26 volumetric water content at five different depths. The permafrost data consist of the
27 ground temperature at twenty different depths up to 28.4 m. The high-quality and
28 long-term datasets are expected to serve as accurate forcing data in land surface
29 models and evaluate remote-sensing products for a broader geoscientific community.
30 The datasets are available from the National Tibetan Plateau/Third Pole Environment
31 Data Center (<https://doi.org/10.11888/Cryos.tpdc.271838>, Wu and Xie, 2021).

32 **1 Introduction**

33 Permafrost is defined as ground that remains at or below 0 °C for at least two
34 consecutive years (Van Everdingen, 1998). As a major component of the cryosphere,
35 the area underlain by permafrost ranges from $12.21 \times 10^6 \text{ km}^2$ to $16.98 \times 10^6 \text{ km}^2$, or
36 from 12.8% to 17.8% of the terrestrial landscape in the Northern Hemisphere (Zhang
37 et al., 2000). The active layer, which is the top layer of the ground subject to annual
38 thawing and freezing in areas underlain by permafrost, plays an important role in cold
39 regions because most ecological, hydrological, biogeochemical, and pedogenic
40 activities take place within it (Hinzman et al., 1991; Kane et al., 1991; Nelson et al.,
41 2000). The thermal state of permafrost is sensitive to climatic warming. There are
42 increasing evidences indicate that permafrost is warming at both global and regional

43 scales (Harris et al., 2003; Cheng and Wu, 2007; Romanovsky et al., 2010; Zhao et al.,
44 2010; Hjort et al., 2018; Biskaborn et al., 2019). Generally, the evidence of permafrost
45 degradation includes rising mean annual ground temperature, deepening active layer
46 thickness, talik and thermokarst development, and decreasing permafrost extent
47 (Cheng and Wu, 2007). Permafrost degradation affects local hydrology, ecosystems,
48 infrastructure stability, and even feedbacks to the climate system (Nauta et al., 2015;
49 Walvoord and Kurylyk, 2016; Hjort et al., 2018; Wang et al., 2021; Zhang et al., 2021;
50 Shogren et al., 2022).

51 Relict permafrost is usually characterized by high-temperature sporadic
52 permafrost, where the mean annual ground temperature of permafrost is close to 0 °C.
53 The relict permafrost presents a favourable opportunity to compare the impacts of
54 climatic warming on the permafrost and the seasonal frozen ground, as they have
55 similar climate conditions (Mu et al., 2017). In addition, the different impacts of
56 vegetation, terrain, and organic matter on the ground thermal regime could be
57 determined in the relict permafrost regions (Xie et al., 2013). Long-term and
58 continuous observations of meteorological variables, active layer, and permafrost are
59 of great importance to understanding the impacts of climatic changes on the ground
60 thermal regime. It is critical to better understand the energy balance at the ground
61 surface to enhance our understanding of the heat and moisture exchanges within the
62 active layer and the permafrost layer. Furthermore, the data on atmospheric conditions
63 and hydrothermal regimes of the active layer are also of great significance for
64 validating remote sensing datasets and land surface models in cold regions
65 (Westermann et al., 2011; Park et al., 2016; Park et al., 2018; Che et al., 2019; Zhao et
66 al., 2021a). However, on the Qinghai-Tibet Plateau, high-quality and long-term
67 datasets of meteorological and permafrost data are relatively scarce, especially in the
68 relict permafrost regions, due to limited logistic support, expensive maintenance costs,
69 and difficult living environments (Li et al., 2020). It is of great importance to share
70 the good data for addressing the challenges of climate change and its impacts on
71 permafrost (Li et al., 2021a). In this paper, the presented data include hourly
72 meteorological variables, daily soil temperature and soil volumetric water content,

73 monthly permafrost temperature, and soil physical parameters from the relict
74 permafrost site at the Mahan Mountain.

75 The Mahan Mountain relict permafrost is located on the northeast Qinghai-Tibet
76 Plateau, which is the peak of the Chinese Loess Plateau and discovered by Li (1986)
77 in fractured bedrock on the Mahan Mountain. It is the only region in the Loess Plateau
78 (China) where permafrost exists. Due to the high mean annual temperature in this
79 region, the permafrost existence can be mainly attributed to two mechanisms. First,
80 the peat layer protects the permafrost from thawing. The organic carbon-rich layer can
81 prevent heating from the air during the warm season as well as the heat loss during the
82 cold season (Du et al., 2012). Second, the high content of ground ice can also favour
83 the presence of the permafrost. It is well known that the phase change of ground ice
84 can absorb a large amount of heat, and thus, the ground temperature will not change
85 significantly in warm permafrost (Biskaborn et al., 2019). In addition, the frequent
86 foggy weather in the area may also decrease the solar radiation and thus favour the
87 presence of permafrost. The characteristics and persistence of the relict high-altitude
88 permafrost on the Mahan Mountain have been demonstrated by Xie et al. (2013).

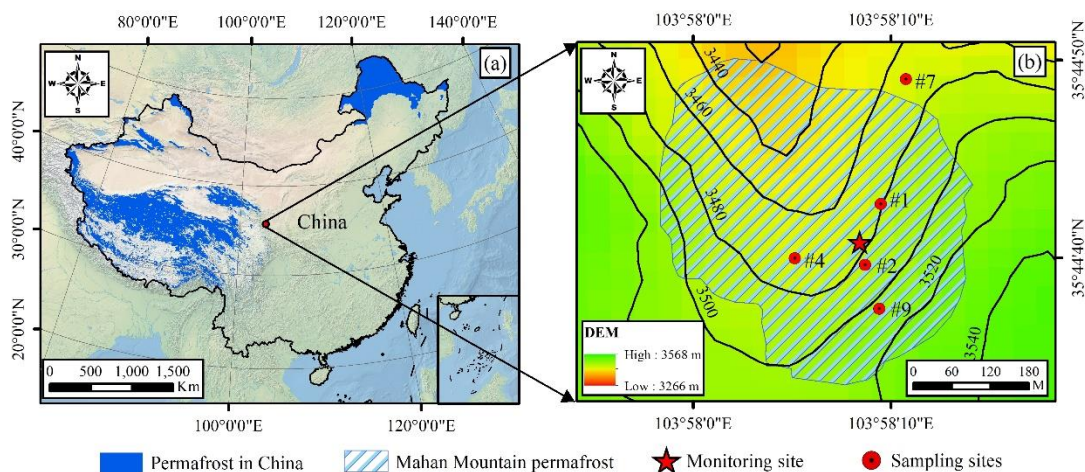
89 We present standard meteorological data, including air and land surface
90 temperature, relative humidity, water vapor pressure, wind speed and direction,
91 shortwave downwards and upwards radiation, longwave downwards and upwards
92 radiation, and precipitation. The data cover an 11-year span from January 1, 2010, to
93 December 31, 2020. In addition, field measurements for soil physical parameters at
94 different depths of five sampling sites from October 2015 to August 2016 are also
95 presented, including soil bulk density, soil gravimetric water content, and soil
96 porosity.

97 **2 Data description**

98 **2.1 Site description**

99 The Mahan Mountain relict permafrost observation site (35°44'N and 103°58'E,
100 3670 m a.s.l.) was established in 2009 by the Cryosphere Research Station on the
101 Qinghai-Tibet Plateau, the Northwest Institute of Eco-Environment and Resource, the

102 Chinese Academy of Sciences. From 1991 to 1993, Li et al. (1993) drilled 12
 103 boreholes across four transects to evaluate the occurrence of permafrost. Among them,
 104 6 boreholes showed obvious evidence indicating permafrost occurrence. The
 105 permafrost mostly emerged in the moist depression regions where vegetation is well
 106 developed. The original permafrost area was approximately 0.16 km², the area of
 107 which has recently been reduced to 0.13 km² (Xie et al., 2013). The mean annual
 108 ground temperature ranges from -0.2 °C to -0.3 °C, which belongs to typical warm
 109 permafrost (Cheng and Wu, 2007). The permafrost thickness is approximately 5–40 m,
 110 and the active layer thickness ranges from 1.0 m to 1.5 m (Li et al., 1993; Dong et al.,
 111 2013; Liu et al., 2015). The existence of an abundant peat layer and ground ice can
 112 exert an effective protective effect on the underlying permafrost. Thus, although the
 113 permafrost extent is very small, the relict permafrost is not sensitive to climate
 114 warming (Xie et al., 2013).



115
 116 **Figure 1.** The location of Mahan Mountain relict permafrost region in China (a), the spatial
 117 distribution of permafrost and monitoring sites in the study region (b). Permafrost distribution data
 118 in China are derived from Zou et al. (2017) and Zhang et al. (2019), and the Environmental and
 119 Ecological Science Data Center for West China (<http://westdc.westgis.ac.cn>). The permafrost
 120 distribution of the Mahan Mountain is derived from Xie et al. (2013). The high-resolution
 121 satellite-derived land cover data are provided by Natural Earth (<http://www.naturalearthdata.com>).

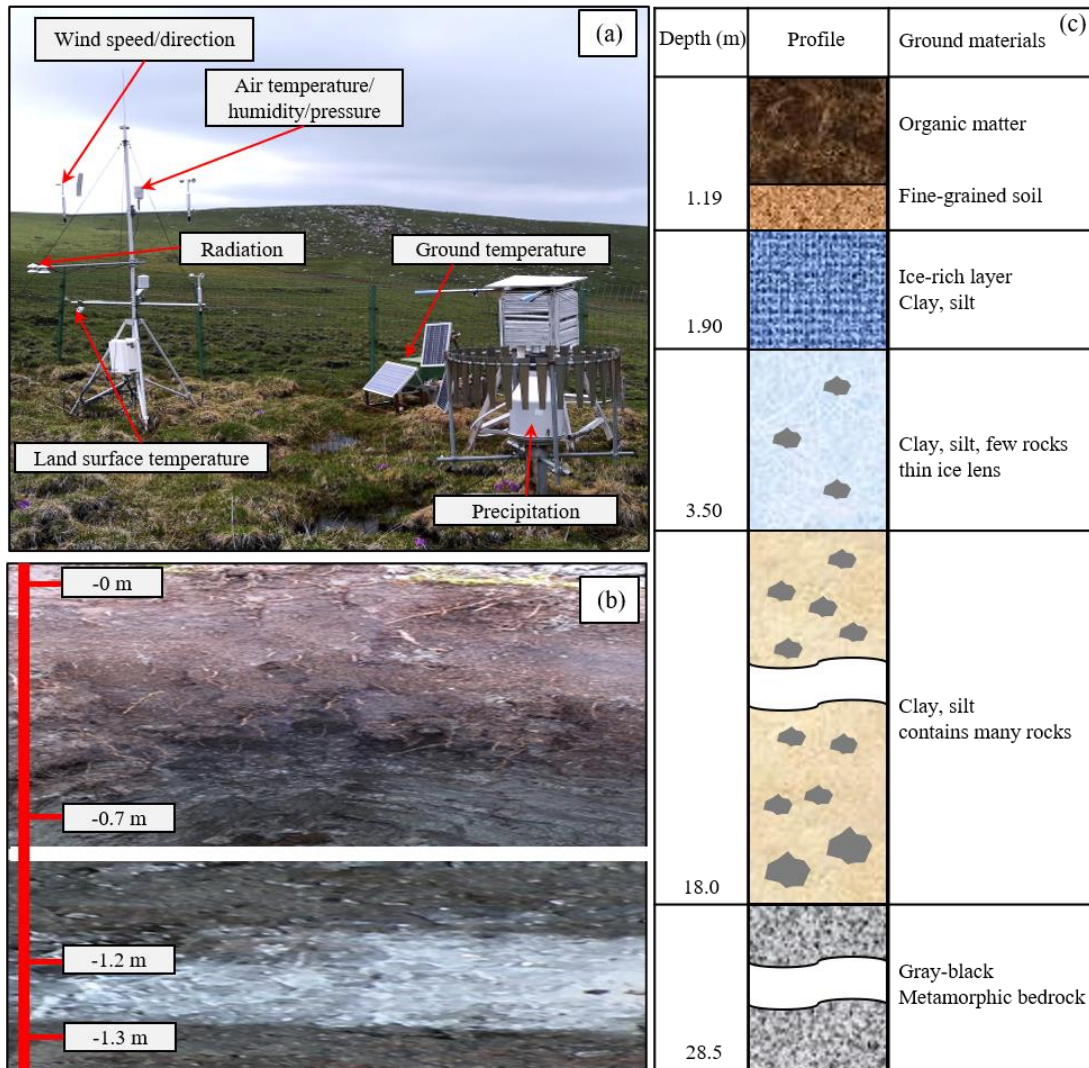
122 The climate conditions on the Mahan Mountain are cold and subhumid. The
 123 observed mean annual air temperature in the relict permafrost region is approximately
 124 -1.4 °C from 2010 to 2020, and the duration of negative air temperature exceeds 200

125 days. The local ground surface is covered by the swamp meadow with approximately
126 90% coverage. The dominant plant types mainly include *Kobresia humilis*, *K.*
127 *pygmaea*, and *K. capilifolia* (Sun and Zhao, 1995). Abundant hummocks are well
128 developed and are influenced by high moisture contents and frost heaving effects. A
129 greater ecosystem respiration rate and soil carbon release occurred in the relict
130 permafrost region than in the Arctic permafrost region (Mu et al., 2017).

131 **2.2 Data description**

132 The Mahan Mountain meteorological and permafrost observation sites were set
133 up in 2009. The observation details are shown in Fig. 2 and Table 1. There is regular
134 manual maintenance every one or two months, mainly including power system
135 checking, sensor and field cleaning, and data collection. In addition, to prevent the
136 thermistors in the borehole from shifting during the monitoring period, we set up a
137 steel wire running through the borehole, and a cable wrapped with thermistors is fixed
138 to the steel wire, which can ensure that the cable is vertical and prevent the
139 thermistors from moving in the borehole. We also calibrate these thermistors every
140 year at the State Key Laboratory of Frozen Soil Engineering, Chinese Academy of
141 Sciences. However, for the sensors in the active layers, we cannot calibrate the depths
142 of all sensors every year, which may lead to some errors. Moreover, due to the
143 independent power energy from three solar panels, the meteorological data were
144 continuous with high quality.

145 For the active layer soil temperature and soil water content observations, there
146 were several blank gaps from 2012 to 2014 owing to a broken storage battery.
147 Subsequently, we solved these problems by installing a new storage battery with a
148 larger capacity. Moreover, the permafrost borehole suffered water penetration from
149 2012 to 2016, which caused low-quality permafrost temperature data; we repaired it
150 and manually measured the permafrost temperature at different depths since 2017.
151 The related data introduction is as follows.



152

153 **Figure 2.** The setup of the meteorological and permafrost observation site on the Mahan Mountain.

154 The meteorological monitoring parameters mainly include wind speed and direction, air humidity,

155 radiation, land surface temperature (LST), and precipitation (a); active layer soil profile and

156 ground ice near the permafrost table (b); and soil profile information of the permafrost borehole

157 (c). Figure 2a was recorded on June 15, 2020. Note that we selected flat ground with

158 homogeneous vegetation type to set up the instruments. After some instruments were destroyed by

159 animals, so we set up a fence to protect the instruments. There were slight differences in the

160 vegetation biomass during the following years.

161 2.2.1 Meteorological conditions

162 The meteorological station of the Mahan Mountain continues to observe a

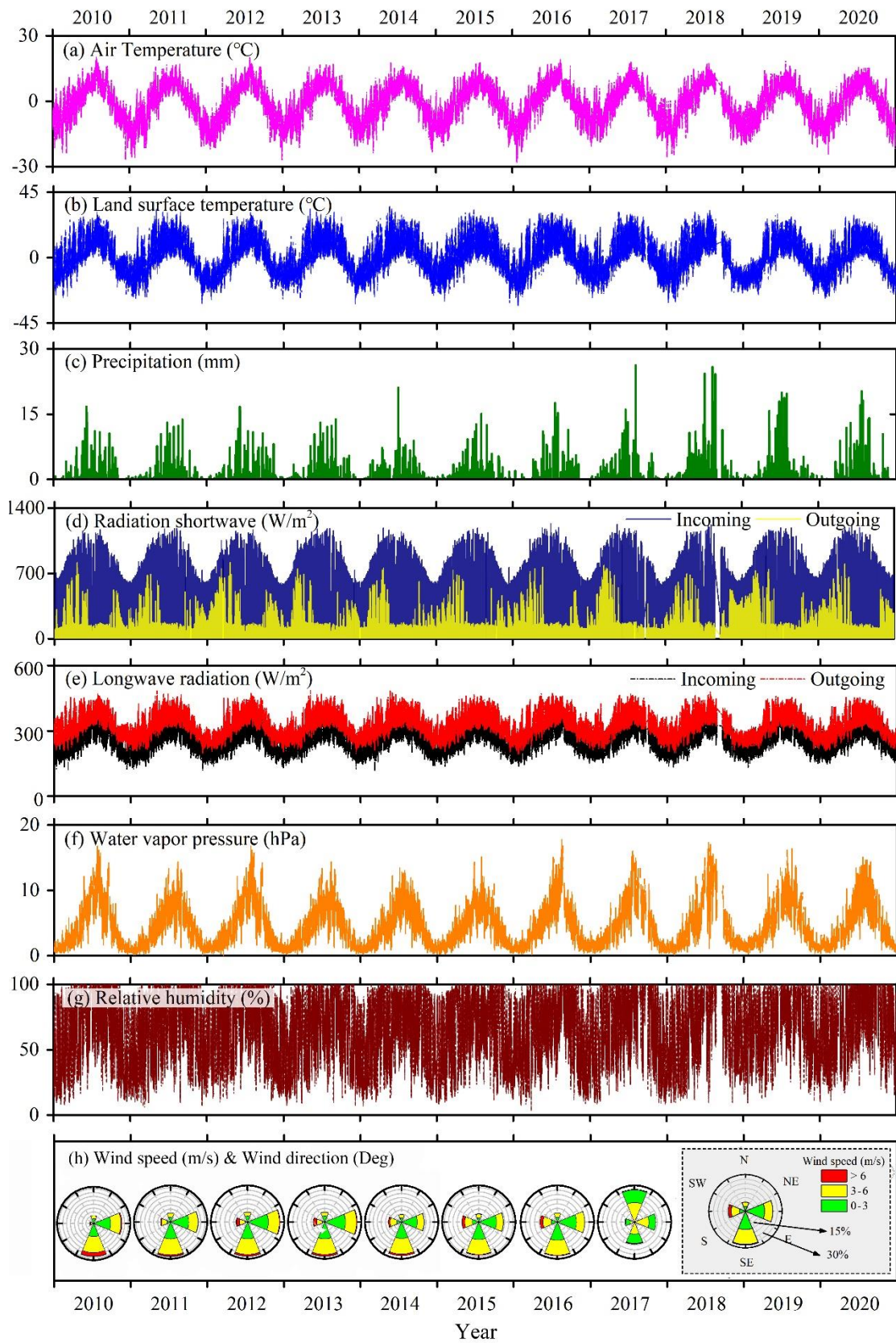
163 variety of meteorological variables from January 1, 2010, to December 31, 2020

164 (Table 1). All meteorological variables are monitored in 30-minute intervals (Fig. 2),

165 and the monitoring data are recorded by a CR1000 data logger (Campbell Scientific,
 166 Inc.). Because the weather observation equipment is regularly maintained, most of the
 167 meteorological data have high quality and continuity with very limited missing data.
 168 The detailed description of each meteorological variable is presented as following
 169 (Table 1).

170 **Table 1.** List of sensors, accuracy, measuring height, measuring interval, and operation period for
 171 meteorological variables at the Mahan Mountain from January 2010 to December 2020.

Variable	Sensor	Range	Accuracy	Sensor height	Measuring interval	Unit
Shortwave radiation	CM3, Kipp & Zonen, Netherlands	0 to 2000 W/m ²	<5%	2m	30min	W/m ²
Longwave radiation	CM3, Kipp & Zonen, Netherlands	0 to 2000 W/m ²	<10%	2m	30min	W/m ²
Air temperature	HMP45C,Vaisala Finland	-40 to 60 °C	±0.2-0.5 °C	2m, 4m	30min	°C
Relative humidity	HMP45C,Vaisala Finland	0 to 100 % RH	±3%	2m, 4m	30min	%
Wind speed/direction	014A, MetOne, USA	0 to 45 m/s	0.11m/s	2m	30min	m s ⁻¹ / Deg
Water vapor pressure	HMP45C,Vaisala Finland	-	±3%	2m, 4m	30min	hPa
Precipitation	T200B3 precipitation gauge	0 to 1000 mm	0.1%	1.6m	1 day	mm
Land surface temperature	IRR-P,Vaisala Finland	-55 to 80 °C	±0.3 °C	2m	30min	°C



172

173 **Figure 3.** Time series of meteorological variables from 2010 to 2020 at the Mahan Mountain,
 174 including air temperature at 2 m height (a), land surface temperature (b), precipitation at 1.6 m

175 height (c), shortwave radiation at 2 m height (d), longwave radiation at 2 m height (e), water vapor
176 pressure at 4 m height (f), relative humidity at 4 m height (g), wind speed & direction at 2 m
177 height (h). The temporal resolution of precipitation data is daily scale, and hourly scale for other
178 all variables.

179 **Air and land surface temperature**

180 Air temperature was measured by a shielded HMP45C at heights of 2 m and 4 m
181 above the ground surface. Such sensors were relatively stable, and the data integrity
182 reached to almost 100% with an accuracy of 0.2–0.5 °C. During 2010–2020, the mean
183 annual air temperature at 2 m height ranged from -2.0 °C to -0.7 °C (Fig. 3a).
184 Moreover, the annual variations in air temperature amplitudes were approximately
185 38.6–47.7 °C (Fig. 3a).

186 The land surface temperature (LST) was measured by the IRR-P at a height of 2
187 m above the ground surface through noncontact infrared radiation. At the Mahan
188 Mountain permafrost site, the LST ranged from -33.2 °C to 36.9 °C. The lowest mean
189 annual LST was -2.1 °C in 2012, while the highest mean annual LST was -0.6 °C in
190 2016, and the 11-year mean LST was -1.4 °C (Fig. 3b).

191 **Precipitation**

192 A Geonor T-200B precipitation gauge (1000 mm capacity) was installed at a
193 height of 1.6 m above the ground surface. There is a vibrating-wire sensor within the
194 gauge to measure the total weight of a collection bucket, and a single Alter shield
195 around the gauge can guarantee a higher catch ratio to some extent. In general, the
196 accuracy and sensitivity of this gauge are 0.1% and 0.1 mm, respectively. This gauge
197 has been widely used to as the reference standard in the WMO Solid Precipitation
198 Intercomparison Experiment (WMO-SPICE) (Nitu et al., 2018) and related
199 precipitation intercomparison experiments (Zhao et al., 2021b). Due to the influence
200 of wind disturbance, wetting loss and evaporation loss, some abnormal precipitation
201 values exist. To guarantee the data quality, we have checked related records to decide
202 whether a precipitation event occurred by combining synchronous air temperature and

203 land surface temperature, shortwave radiation, relative humidity data, and related data
204 were also corrected according to the reference of Domine et al. (2021).

205 The observed local annual total precipitation was 318.6 ± 54.3 mm from 2010 to
206 2020, and the minimum and maximum annual total precipitation occurred in 2015 and
207 2018 with values of 258.3 mm and 443.9 mm, respectively (Fig. 3c). In addition,
208 approximately 80% of the annual precipitation is concentrated in the period of May to
209 September, and only no more than 5% of the precipitation occurs in winter.

210 **Radiation**

211 Upwards/downwards shortwave and longwave radiations were measured by the
212 Kipp & Zonen CM3 radiometer. The spectral ranges of the shortwave and longwave
213 radiometers are from 0.3 μm to 2.8 μm and from 4.5 μm to 42 μm , respectively. On
214 the Mahan Mountain, the downwards shortwave radiation tended to reach its
215 maximum in spring, followed by summer, and was lowest in winter and autumn.
216 Upwards shortwave radiation also reached its maximum in spring, but the difference
217 was that the downwards shortwave radiation in summer was comparable to that of
218 autumn and winter, or even lower, which was mainly due to the cloudy and rainy
219 weather in summer. The maximum values of upwards/downwards longwave radiation
220 usually occurred in summer, followed by autumn, while the values in winter and
221 spring tended to be lower, which shows similar patterns with the seasonal variations
222 in land surface temperature and air temperature.

223 **Relative humidity and water vapor pressure**

224 The relative humidity was measured by shielded HMP45C probes at heights of 2
225 m and 4 m above the ground surface. However, when in heavy rainfall or fog weather,
226 the observed relative humidity might exceed its physical limits, i.e., 100%. In this
227 case, the relative humidity was corrected to 100% instead (Fig. 3g). The variations in
228 relative humidity were consistent with rainfall events and the variations in air
229 temperature.

230 The water vapor pressure was calculated from the relative humidity at heights of

231 2 m and 4 m above the ground surface. Water vapor pressure generally reached its
 232 maximum in summer, followed by autumn, and lowest in spring and winter, which
 233 showed obvious seasonal variations (Fig. 3f).

234 **Wind speed and wind direction**

235 The 014A MetOne wind speed and direction sensors were installed at a height of
 236 2 m above the ground surface. The negative values for wind directions were replaced
 237 by 6999. The wind speed and direction during 2010–2017 were continuous with high
 238 quality. Extensive data gaps emerged in the wind direction due to equipment problems
 239 after August 27, 2017. The wind speed data gradually became unavailable after 2019.
 240 The wind speed mainly stayed between 2 m/s and 6 m/s (Fig. 3h).

241 **2.2.2 Active layer hydrothermal conditions**

242 **Soil temperature and soil volumetric water content**

243 The underground soil temperature and soil volumetric water content data in the
 244 active layer were monitored at five depths (10 cm, 30 cm, 80 cm, 100 cm, and 120
 245 cm). The soil temperature were measured by 105T/109 thermistors (Campbell
 246 Scientific, USA) with an accuracy of ± 0.1 °C. The soil volumetric water content were
 247 measured by the time-domain reflectometry (TDR-100, Campbell Scientific, USA)
 248 with an accuracy of ± 0.03 . These sensors were all attached to a CR1000 data logger
 249 (Campbell Scientific, USA) at 30-minute intervals. We finally resampled the
 250 30-minute soil temperature and soil volumetric water content data into daily data by
 251 averaging the half-hourly data within a day.

252 **Table 2.** List of sensors, accuracy, measuring height and interval, and operation period for soil
 253 temperature and soil volumetric water content within the active layer at the Mahan Mountain
 254 satiation.

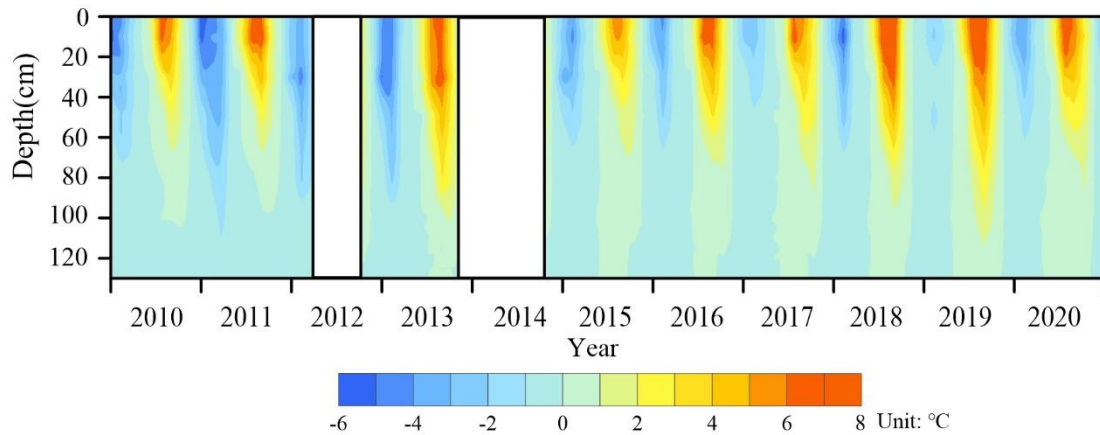
Variable	Sensor	Range	Accuracy	Depth/cm	Measuring interval	Operation period	Unit
----------	--------	-------	----------	----------	--------------------	------------------	------

Soil temperature	105T, Campbell	-78 to +50	± 0.1	10, 30, 80, 100, 120	30min	Jan 2010 – Dec 2020	$^{\circ}\text{C}$
Soil volumetric water content	TDR-100, Campbell	0 to 1	± 0.03	10, 30, 80, 100, 120	30min	Jan 2010 – Dec 2020	m^3m^{-3}

255 To obtain highly accurate data, quality control was performed by manually
256 checking whether there were abnormal or missing data. For the soil temperature data,
257 the missing data accounted for 17.1% during the period of 2010–2020. The major soil
258 temperature data gaps were from November 23, 2013, to September 21, 2014. In
259 addition, we checked the soil temperature data based on the zero-curtain effect,
260 assuming that the soil properties and water composition did not change during 2010–
261 2020. For the soil volumetric water content data, the missing and abnormal data
262 accounted for approximately 30.7% of the entire soil volumetric water content data,
263 mainly from 2012 to 2014. If the soil volumetric water content data were only missing
264 in several hours within a day, we interpolated the missing data with the proximity
265 averaging method. In the case of missing data persisting for a longer time, we filled
266 them with 6999. Overall, all the missing or abnormal soil temperature and soil
267 volumetric water content data were replaced with 6999.

268 According to the soil temperature profile (Fig. 4), the soil temperature in the
269 active layer shows a seasonal dynamic change. The thawing onset was generally in
270 the middle of April, and the maximum thawing depth was reached in late September.
271 The amplitude of the ground temperature in the active layer decreased rapidly with
272 increasing soil depth. The minimum and maximum values of the soil temperature data
273 at depths of 10 cm, 30 cm, 80 cm, 100 cm, and 120 cm were $-8\text{ }^{\circ}\text{C}$ and $9.8\text{ }^{\circ}\text{C}$, $-6.4\text{ }^{\circ}\text{C}$
274 and $8.4\text{ }^{\circ}\text{C}$, $-3.1\text{ }^{\circ}\text{C}$ and $3.5\text{ }^{\circ}\text{C}$, $-1.4\text{ }^{\circ}\text{C}$ and $1.9\text{ }^{\circ}\text{C}$, and $-0.74\text{ }^{\circ}\text{C}$ and $0.7\text{ }^{\circ}\text{C}$,
275 respectively. The mean annual soil temperature in 2019 reached its maximum during
276 2010–2020. Under the influence of the freeze–thaw process, the thermal state of the
277 active layer is not constant during the whole year. In addition, the difference in
278 thermal conductivity between the frozen and thawed ground causes a "negative
279 thermal offset", which is defined as the difference between the mean annual soil

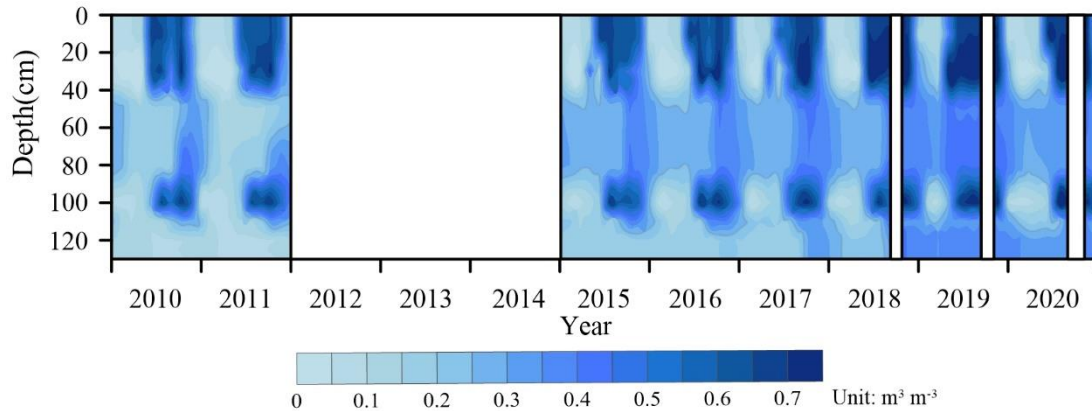
280 temperature at the bottom of the active layer (TTOP) and the mean annual soil surface
 281 (~0 cm) temperature (MAGST) (Burn and Smith, 1988). In this study, the value of
 282 MAGST is larger than +0.97 °C (MAST at 10 cm). Therefore, the thermal offset =
 283 TTOP - MAGST= -0.1 °C - (> +0.97 °C) > -1.07 °C. This result is consistent with the
 284 general understanding of thermal offset in the permafrost regions (Romanovsky and
 285 Osterkamp, 1995).



286
 287 **Figure 4.** Active layer soil temperature profiles during 2010–2020 at the Mahan Mountain
 288 permafrost site. The blank gap stands for the missing data.

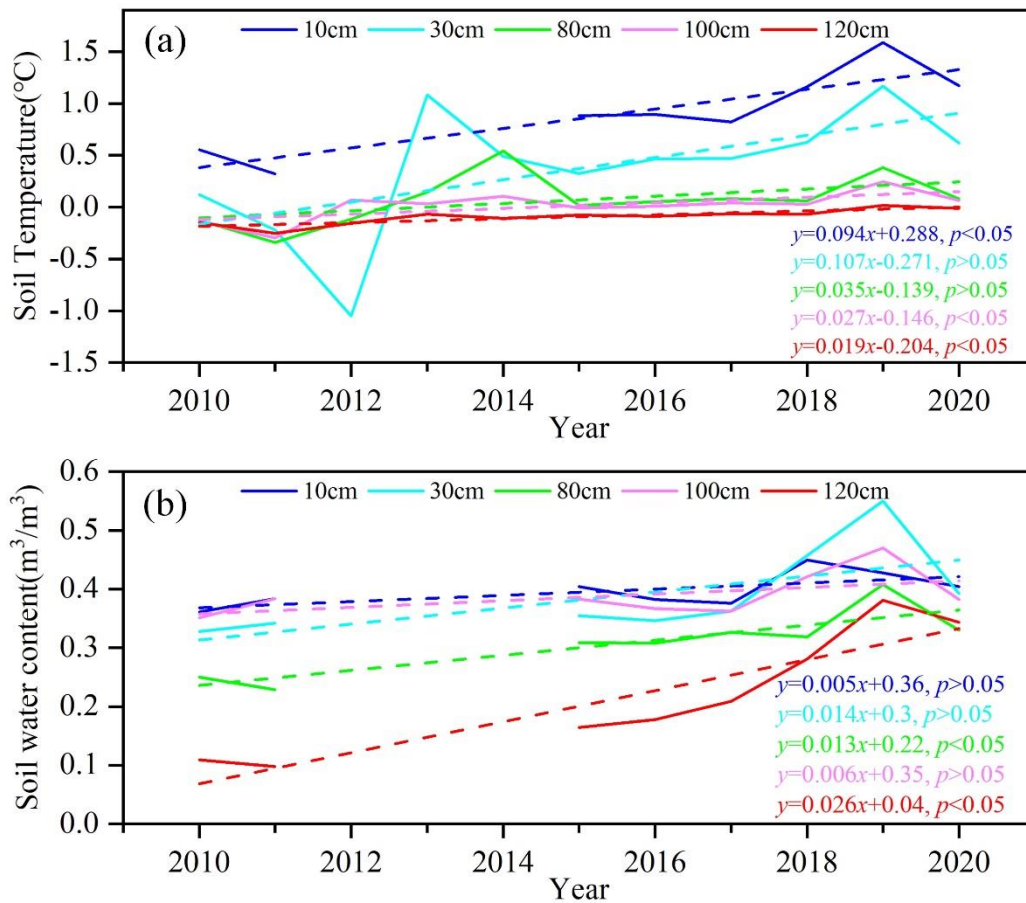
289 As shown in Fig. 5, there were two higher soil volumetric water content zones in
 290 the upper and lower parts of the active layer, which were located at approximately 0–
 291 40 cm and 90–110 cm depths, respectively, and a relatively lower soil volumetric
 292 water content was in the middle part of the active layer. The distribution of abundant
 293 vegetation and peat layers, soil particle fractions, the freeze–thaw process, the ground
 294 ice layer, water channels such as soil pores, and cracks can affect soil water contents.
 295 These factors may account for the abnormal features of soil water contents at the
 296 depths of 40–80 cm and 100 cm (Hincapi é and Germann, 2009; Xu et al., 2010; Hu et
 297 al., 2014; Mathias et al., 2015; Zhu et al., 2017). In the thawing season, the soil
 298 volumetric water content reached approximately $0.7 \text{ m}^3 \text{ m}^{-3}$ in the upper and lower
 299 parts of the active layer, and was approximately $0.3 \text{ m}^3 \text{ m}^{-3}$ to $0.4 \text{ m}^3 \text{ m}^{-3}$ in the middle
 300 part of the active layer. In the freezing season, there were significant differences from
 301 the thawing season, and the soil volumetric water content in the middle part of the
 302 active layer was higher than that of the upper and lower parts of the active layer.

303 Moreover, the soil volumetric water content at 40–90 cm depths exhibited a rapid
 304 increase in the freezing season since 2015, which could reach to $0.4 \text{ m}^3 \text{ m}^{-3}$, and the
 305 soil volumetric water content at around 120 cm depth showed a rapid increase in the
 306 freezing season since 2017, with a slightly lower soil volumetric water content than
 307 that of the 40–90 cm depths.



308
 309 **Figure 5.** Evolution of soil volumetric water content profiles from 2010 to 2020 at the Mahan
 310 Mountain permafrost site. The blank gap stands for the missing data.

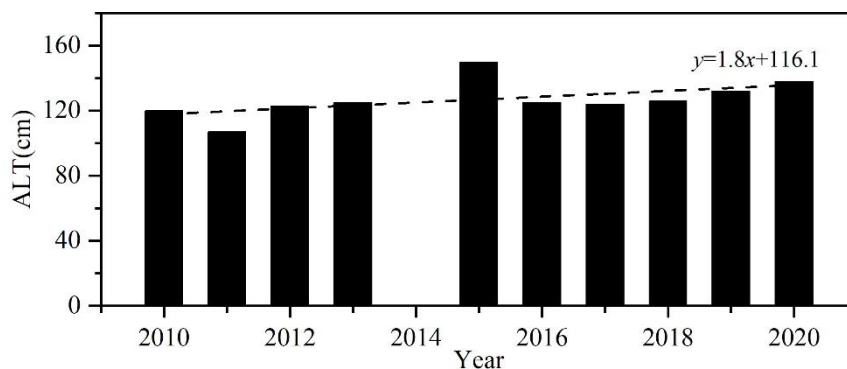
311 The results revealed that the average warming rate of soil temperature at different
 312 depths was $0.056 \text{ }^\circ\text{C}/\text{year}$ at the Mahan Mountain from 2010 to 2020 (Fig. 6a). The
 313 highest warming rate of soil temperature was $0.107 \text{ }^\circ\text{C}/\text{year}$ at a depth of 30 cm,
 314 while the lowest value was $0.019 \text{ }^\circ\text{C}/\text{year}$ at a depth of 120 cm (Fig. 6a). The average
 315 changing trend of the volume soil water content was $0.013 \text{ m}^3 \text{ m}^{-3}/\text{year}$ from 2010 to
 316 2020, and the highest value was $0.026 \text{ m}^3 \text{ m}^{-3}/\text{year}$ at a depth of 120 cm, while the
 317 lowest value was $0.005 \text{ m}^3 \text{ m}^{-3}/\text{year}$ at a depth of 10 cm (Figure 6b).



318

319 **Figure 6.** Soil temperature and soil volumetric water content at five depths from 2010 to 2020 at
 320 the Mahan Mountain permafrost site: soil temperature (a), soil volumetric water content (b).

321 The active layer thickness (ALT) varied between 107 cm and 150 cm with a
 322 mean value of 127 cm from 2010 to 2020 (Fig. 7). The rate of change in ALT was 1.8
 323 cm/year. The increasing rates of ALT in recent decades have varied considerably in
 324 different permafrost regions (Table 5).



325

326 **Figure 7.** The active layer thickness (ALT) from 2010 to 2020 at the Mahan Mountain permafrost

327 site. The ALT data in 2014 were not available.

328 **Soil physical parameters**

329 From October 2015 to August 2016, field measurements of soil physical
330 parameter data were carried out by test pit probing and sampling soils, including soil
331 gravimetric water content, soil bulk density, and soil porosity. There were five
332 sampling sites in total. Four sites (#1, #2, #4, and #9) are located in the permafrost
333 region, where the vegetation type is dominated by swamp meadow. Site #7 is located
334 in a seasonally frozen ground region, where the vegetation type is mainly alpine
335 meadow (Table 3). These data can be used as the input parameters in relevant
336 permafrost and land surface process models.

337 **Table 3** Information on the field sampling site for the soil physical parameters from October 2015
338 to August 2016 at the Mahan Mountain.

Sampling site	Elevation (m)	Vegetation type	Frozen soil type
#1	3576.4	Swamp meadow	Permafrost
#2	3576.9	Swamp meadow	Permafrost
#4	3577.2	Swamp meadow	Permafrost
#7	3567.0	Alpine meadow	Seasonally frozen ground
#9	3578.7	Swamp meadow	Permafrost

339 Soil samples were obtained in each soil layer using a standard soil sampler (5 cm
340 diameter and 5-cm-high stainless-steel cutting ring). The soil bulk density is estimated
341 using the oven-dry method. Soil porosity is the ratio of nonsolid volume to the total
342 volume of soil, which is calculated by the soil bulk density and specific weight of the
343 soil (Zhao and Sheng, 2015; Indoria et al., 2020). As shown in Table 4, the soil bulk
344 density and soil porosity at sites #4, #7, and #9 presented significant differences at
345 different depths. Site #7, which is located in the seasonally frozen ground, shows a
346 larger soil bulk density ranging from 0.66 g/cm³ to 1.27 g/cm³. As the soil depth
347 increased, the soil bulk density of sites #4 and #7 increased. Soil porosity also showed
348 obvious differences among the three sites, whereas the shallow soil layers exhibited

349 greater porosity than the deep soil layers. The soil porosity of site #4 ranges from 69.7%
 350 to 85.5%, where the maximum values are found at depths of 0–40 cm.

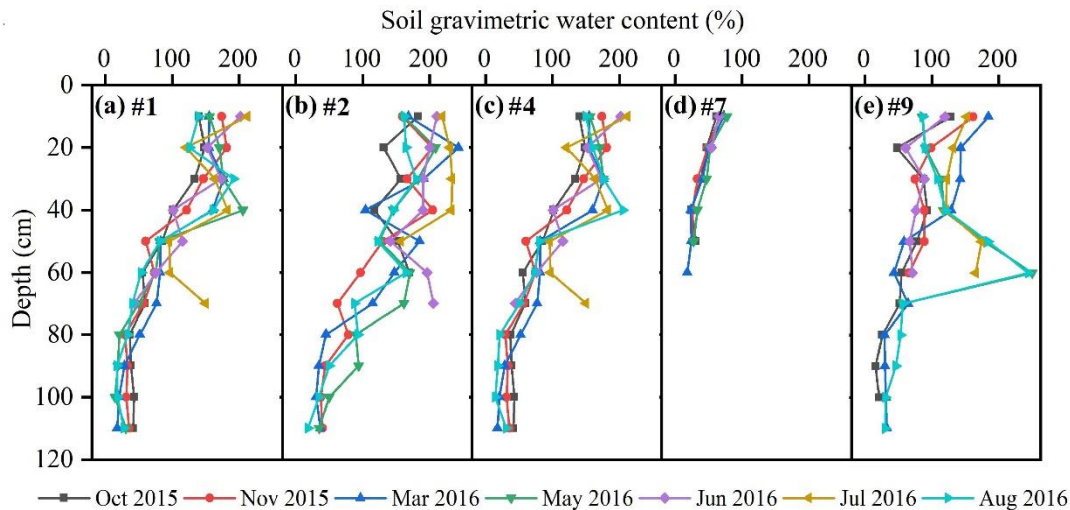
351 **Table 4** Soil bulk density and soil porosity within the active layer at different depths from October
 352 2015 to August 2016 at the Mahan Mountain. The location and information of the sampling sites
 353 are shown in Figure 1(b) and Table 3, respectively.

Depth (cm)	Soil bulk density (g/cm ³)			Soil porosity (%)		
	#4	#7	#9	#4	#7	#9
0–10	0.34	0.66	0.45	85.5	74.3	81.0
10–20	0.56	0.92	0.53	76.0	65.4	76.9
20–30	0.41	0.84	0.55	81.1	68.4	75.6
30–40	0.37	1.03	0.56	84.5	61.8	74.5
40–50	0.67	1.27	0.43	74.7	53.4	76.3
50–60	0.82	null	0.46	69.7	null	83.9
60–70	0.62	null	0.45	77.1	null	83.1

354

Note: “null” stands for no samples.

355 Moreover, the gravimetric soil water content (GWC) was measured by using the
 356 oven drying method (Zhao and Sheng, 2015). The GWC is the ratio between the
 357 absolute weights of wet and dry soil samples, which can be measured after drying for
 358 24 h at 105 °C. The GWC at the five sites showed similar profile features. Overall, the
 359 GWC gradually decreased with increasing soil depth (Fig. 8). The GWC at the four
 360 permafrost sites (#1, #2, #4, and #9) shows similar patterns in depth, with their values
 361 ranging from 15% to 250%. The GWC at the seasonal frozen ground site (#7) is only
 362 18.5–77.4%, which is smaller than that at the four permafrost sites (Fig. 8d). In
 363 addition, GWC also presents some monthly differences, such as larger values tending
 364 to occur in June and July in the 10–40 cm layers, which may be caused by abundant
 365 precipitation and thawing processes during this period. The abnormally high value at
 366 a depth of 60 cm at site #9 during August 2016 is likely related to the existence of
 367 subsurface flow.



368

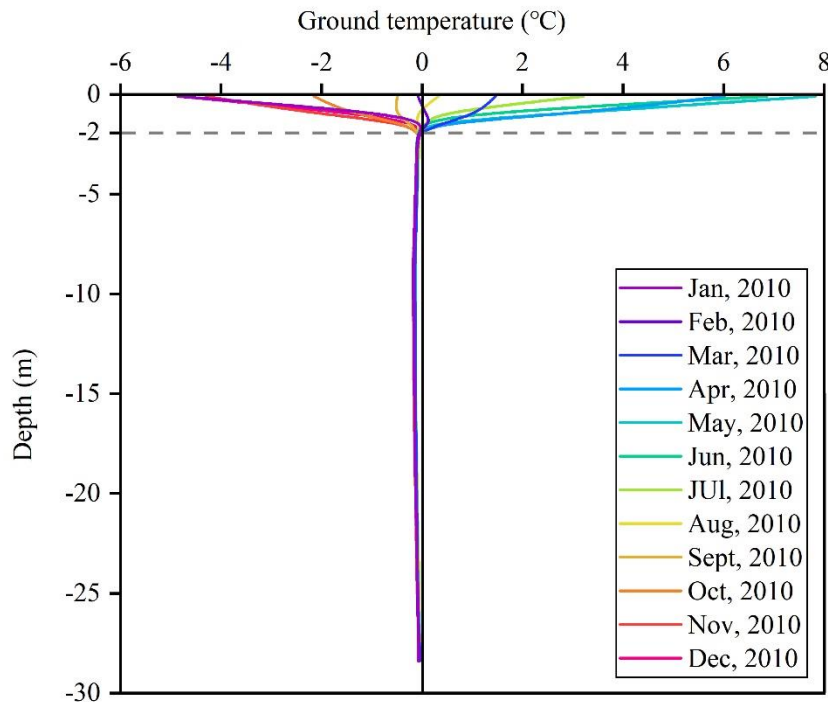
369 **Figure 8.** Soil gravimetric water content at five sampling sites (#1, #2, #4, #7, and #9) from
 370 October 2015 to August 2016 at the Mahan Mountain permafrost region. The location and
 371 information of the sampling sites are shown in Figure 1(b) and Table 3, respectively.

372 **2.2.3 Permafrost temperature**

373 In August 2008, a borehole with a depth of 28.5 m was drilled to monitor the
 374 permafrost temperature. In mid-December 2008, twenty thermistors were installed at
 375 different depths in the borehole (0.1 m, 0.4 m, 0.9 m, 1.4 m, 1.9 m, 2.4 m, 3.4 m, 6.4
 376 m, 7.4 m, 9.4 m, 11.4 m, 13.4 m, 15.4 m, 17.4 m, 19.4 m, 21.4 m, 23.4 m, 25.4 m,
 377 27.4 m, and 28.4 m). Thermistor probes made by the Chinese State Key Laboratory of
 378 Frozen Soil Engineering at Lanzhou were used to measure the ground temperature.
 379 These thermistor probes have a sensitivity of ± 0.05 °C in the lab (Cheng and Wu,
 380 2007). From May 2009, permafrost temperature data for each half-hour were
 381 automatically recorded by the datalogger (CR1000, Campbell Scientific, USA). No
 382 data were recorded from 2012 to 2016 due to water penetration into the borehole.
 383 Since 2017, a digital multimeter has been used to manually measure the permafrost
 384 temperature at 13 layers (3 m, 4 m, 5 m, 7 m, 9 m, 11 m, 13 m, 15 m, 17 m, 19 m, 21
 385 m, 23 m, and 25 m) for 2–4 times each month. Quality control was carried out to
 386 check whether the data were missing or invalid, which was replaced by 6999 as no
 387 data. The ground temperature is then resampled to monthly data.

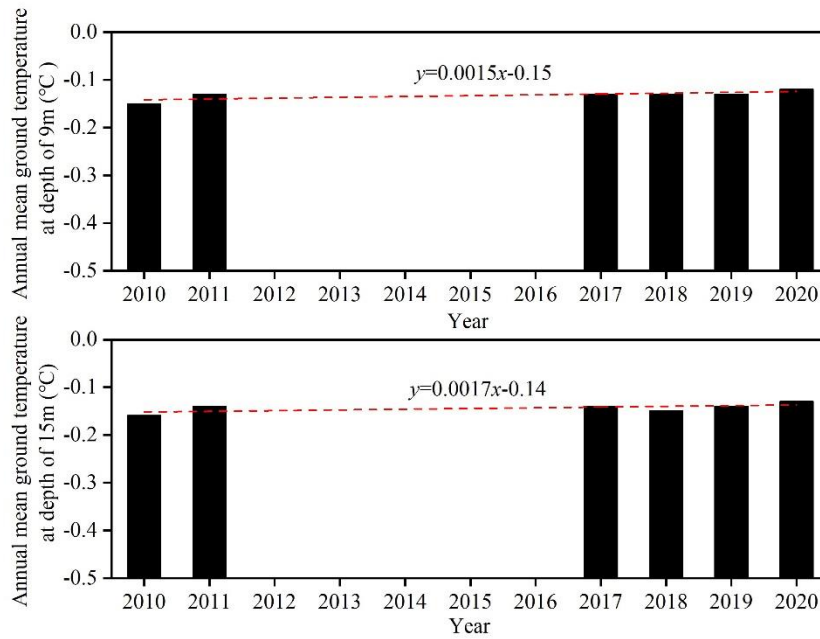
388 The records showed that the permafrost temperature at all depths below 2 m was

389 mostly negative all year round. The location of the permafrost base at this site
 390 exceeded the drilling depth (28.5 m). The soil temperature in the permafrost layer
 391 shows minimum values of approximately $-0.2\text{ }^{\circ}\text{C}$ at depths of 10 m to 16 m, close to
 392 $-0.1\text{ }^{\circ}\text{C}$ at depths of -2.4 m to -27.4 m, and increased upwards and downwards with a
 393 temperature gradient of $\pm 0.01\text{ }^{\circ}\text{C}/\text{m}$ (Fig. 9). The permafrost temperature data were
 394 not available during 2012–2016 due to the sensor failure. After 2017, a digital
 395 multimeter was used to manually measure the permafrost temperature for 2–4 times
 396 each month. We calculated the annual average permafrost temperature at depths of 9
 397 m and 15 m. The result shows that the annual mean ground temperature at these
 398 depths only showed slight changes during 2010–2020 (Fig. 10).



399
 400
 401

Figure 9. Ground temperature in the permafrost borehole drilled in 2010 at the Mahan Mountain.



402

403 **Figure 10.** The annual mean ground temperature at depths of 9 m and 15 m during 2010–2020 at
 404 the permafrost site.

405 **2.2.4 Comparison of the variation in permafrost characteristics with other**
 406 **regions**

407 There was an obvious regional difference in the variation in the ALT (Table 5).
 408 The change rate of ALT since the 1990s was less than 1 cm/year in the permafrost
 409 regions of Alaska, northeastern Siberia, and Antarctica, especially in the permafrost in
 410 Canada, which was close to 0 cm/year (Smith et al., 2022). The trends in the
 411 permafrost regions of Nordic, northern Russian European, western and central Siberia,
 412 and the Qinghai-Tibet Plateau are closer to the results of this paper (Zhao et al., 2019;
 413 Smith et al., 2022). The ALT showed the greatest change in permafrost regions of the
 414 Swiss Alps (Table 5). In addition, the permafrost temperature change on the Mahan
 415 Mountain is significantly lower than that of other regions, which usually have a
 416 warming rate greater than 0.15 °C/decade (Table 5). This pattern can be explained by
 417 the existence of a high content of ground ice. The phase change of ground ice can
 418 absorb a large amount of heat, and thus, the ground temperature will not change
 419 significantly in warm permafrost (Nelson et al., 2001; Biskaborn et al., 2019; Ding et

420 al., 2019). Moreover, the changes in ALT and permafrost temperature varied greatly
 421 from different permafrost regions due to the impact of multiple local factors, such as
 422 snow cover, slope aspect, vegetation cover, and soil properties (Ding et al.,2019;
 423 Smith et al., 2022). It is worth noting that the different study periods, and variability
 424 and continuity of the observed data also have an effect on the results.

425 **Table 5** Comparison of the change rates of active layer thickness (ALT) and permafrost
 426 temperature in different permafrost regions.

Variable	Area	Variation rate	Study period	Reference
Active layer thickness	Alaska North Slope	0.2 cm/year	1990–2020	Smith et al., 2022
	Alaska interior	0.9 /year	1990–2020	
	Canada	0.0 /year	1991–2018	
	Nordic (including Svalbard and Greenland)	1.3 cm/year	1990–2020	
	northern Russian			
	European, western and central Siberia	1.3 cm/year	1993–2020	
	northeastern Siberia (including Chuktoka and Kamchatka)	0.5 cm/year	1994–2020	
	Swiss Alps	10.5 cm/year	1990–2018	
	Antarctica	0.1 cm/year	1999–2019	
	Qinghai-Tibet Plateau	2.17 cm/year	2004–2018	
Mahan Mountain	1.8 cm/year	2010–2020	This study	
Permafrost temperature	Arctic continuous permafrost	0.39±0.15 °C/decade	2008–2016	Biskaborn et al., 2019
	Arctic discontinuous permafrost	0.20±0.10 °C/decade	2008–2016	
	Mountain permafrost	0.19±0.05 °C/decade	2008–2016	
	Antarctica permafrost	0.37±0.10 °C/decade	2008–2016	Cheng et al., 2019
	Qinghai-Tibet Plateau	0.15 °C/decade	2005–2017	
Mahan Mountain	0.02 °C/decade	2010–2020	This study	

427 3 Data availability

428 The dataset has been available and can be freely download from the National
 429 Tibetan Plateau/Third Pole Environment Data Center

430 (<https://data.tpdc.ac.cn/en/disallow/c0a65170-d7cc-4a10-b3fd-39f813cd1387/>,
431 <https://doi.org/10.11888/Cryos.tpdc.271838>, Wu and Xie, 2021).

432 **4. Conclusions**

433 The Mahan Mountain is a relict permafrost site on the northeast of the
434 Qinghai-Tibet Plateau where meteorological and active layer hydrothermal data are
435 automatically acquired and the ground temperature data are manually recorded. This
436 site is dedicated to studies of atmosphere–ground surface interactions and permafrost
437 changes. An 11-year time series of meteorological, active layer and permafrost data is
438 provided. These high-quality and long-term observation data can be used for model
439 validation, including permafrost models, e.g., the CryoGRID 3 model (Westermann et
440 al. 2016), and land surface models, e.g., CLM5 and Noah (Li et al. 2021b). The
441 objective of releasing these data is to improve and validate the permafrost models and
442 land surface models, which face great difficulties in modelling mountain permafrost
443 dynamics.

444 **Author contributions**

445 Tonghua Wu designed the research and obtained funding. Changwei Xie and Wu
446 Wang deployed and maintained the instruments. Xiaofan Zhu, Jie Chen, Amin Wen,
447 Dong Wang, Peiqing Lou, Chengpeng Shang, Yune La, Xianhua Wei, Xin Ma and
448 Yongping Qiao analyzed the data and prepared the data files. Ren Li, Xiaodong Wu,
449 and Guojie Hu conducted the field work. Tonghua Wu wrote the paper with inputs
450 from the co-authors and coordinated the analysis and contributions from all
451 co-authors.

452 **Competing interests**

453 The authors declare that they have no conflict of interest.

454 **Acknowledgements**

455 This work was financially supported by the CAS "Light of West China" Program,
456 the National Natural Science Foundations of China (41771076, 41690142,
457 41961144021). We thank in particular Professor Lin Zhao from Nanjing University of

458 Information Science & Technology for his long-term support to maintain the
459 observation.

460 **References**

- 461 Biskaborn, B. K., Smith, S. L., Noetzli, J., Matthes, H., Vieira, G., Streletskiy, D. A.,
462 Schoeneich, P., Romanovsky, V. E., Lewkowicz, A. G., Abramov, A., Allard, M., Boike, J.,
463 Cable, W. L., Christiansen, H. H., Delaloye, R., Diekmann, B., Drozdov, D., Etzelmüller,
464 B., Grosse, G., Guglielmin, M., Ingeman-Nielsen, T., Isaksen, K., Ishikawa, M., Johansson,
465 M., Johansson, H., Joo, A., Kaverin, D., Kholodov, A., Konstantinov, P., Kröger, T.,
466 Lambiel, C., Lanckman, J.-P., Luo, D., Malkova, G., Meiklejohn, I., Moskalenko, N., Oliva,
467 M., Phillips, M., Ramos, M., Britta, A., Sannel, K., Sergeev, D., Seybold, C., Skryabin, P.,
468 Vasiliev, A., Wu, Q., Yoshikawa, K., Zheleznyak, M., and Lantuit, H.: Permafrost is
469 warming at a global scale, *Nat. Commun.*, 10, 264,
470 <https://doi.org/10.1038/s41467-018-08240-4>, 2019.
- 471 Boike, J., Nitzbon, J., Anders, K., Grigoriev, M., Bolshiyarov, D., Langer, M., Lange, S.,
472 Bornemann, N., Morgenstern, A., Schreiber, P., Wille, C., Chadburn, S., Gouttevin, I.,
473 Burke, E., and Kutzbach, L.: A 16-year record (2002–2017) of permafrost, active-layer, and
474 meteorological conditions at the Samoylov Island Arctic permafrost research site, Lena
475 River delta, northern Siberia: an opportunity to validate remote-sensing data and land
476 surface, snow, and permafrost models, *Earth Syst. Sci. Data*, 11, 261–299,
477 <https://doi.org/10.5194/essd-11-261-2019>, 2019.
- 478 Brown, J., Ferrians, O. J., Heginbottom, J. A., and Melnikov, E. S.: Circum-Arctic Map of
479 Permafrost and Ground Ice Conditions, Boulder, CO, National Snow and Ice Data Center,
480 digital media, 1998.
- 481 Burn, C. R., and Smith, C. A. S.: Observations of the "thermal offset" in near-surface mean
482 annual ground temperatures at several sites near Mayo, Yukon Territory, Canada, Arctic,
483 99-104, <https://www.jstor.org/stable/40510685>, 1988.
- 484 Che, T., Li, X., Liu, S., Li, H., Xu, Z., Tan, J., Zhang, Y., Ren, Z., Xiao, L., Deng, J., Jin, R.,
485 Ma, M., Wang, J., and Yang, X.: Integrated hydrometeorological, snow and frozen-ground
486 observations in the alpine region of the Heihe River Basin, China, *Earth Syst. Sci. Data*, 11,
487 1483–1499, <https://doi.org/10.5194/essd-11-1483-2019>, 2019.
- 488 Cheng, G., and Wu, T.: Responses of permafrost to climate change and their environmental
489 significance, Qinghai-Tibet Plateau, *J. Geophys. Res.: Earth Surf.*, 112, 1-10,

490 <https://doi.org/10.1029/2006JF000631>, 2007.

491 Ding, Y., Zhang, S., Zhao, L., Li, Z. and Kang, S.: Global warming weakening the inherent
492 stability of glaciers and permafrost, *Sci. Bull.*, 64(4): 245-253. [https://doi.org/](https://doi.org/10.1016/j.scib.2018.12.028)
493 [10.1016/j.scib.2018.12.028](https://doi.org/10.1016/j.scib.2018.12.028), 2019.

494 Domine, F., Lackner, G., Sarrazin, D., Poirier, M., and Belke-Brea M.: Meteorological, snow
495 and soil data (2013–2019) from a herb tundra permafrost site at Bylot Island, Canadian
496 high Arctic, for driving and testing snow and land surface models. *Earth Syst. Sci. Data*, 13,
497 4331-4348, <https://doi.org/10.5194/essd-13-4331-2021>, 2021.

498 Dong, X., Xie, C., Zhao, L., Yao, J., and Hu, G.: Characteristics of surface energy budget
499 components in permafrost region of the Mahan Mountain, Lanzhou (in Chinese). *J. Glaciol.*
500 *Geocryol.*, 35(2), 320-326, <https://doi.org/10.7522/j.issn.1000-0240.2013.0038>, 2013.

501 Du, R., Peng, X., Frauenfeld, O. W, Sun, W., Liang, B., Chen, C., Jin, H., and Zhao, Y.: The
502 role of peat on permafrost thaw based on field observation, *Catena*, 208: 105772,
503 <https://doi:10.1016/j.catena.2021.105772>, 2022.

504 Harris, C., Mithll, D. V., Isaksen, K., Haeberli, W., Sollid, J. L., King, L., Holmlund, P.,
505 Dramis, F., Guglielmin, M., and Palacios, D.: Warming permafrost in European mountains,
506 *Glob. Planet. Chang.*, 39, 215-225, <https://doi.org/10.1016/j.gloplacha.2003.04.001>, 2003.

507 Hincapié I., and Germann, P. F., Impact of initial and boundary conditions on preferential
508 flow, *Journal of Contaminant Hydrology*, 104(1-4): 67-73,
509 <https://doi:10.1016/j.jconhyd.2008.10.001>, 2009.

510 Hinzman, L. D., Kane, D. L., and Gieck, R. E: Hydrologic and thermal properties of the
511 active layer in the Alaskan Arctic, *Cold Reg. Sci. Technol.*, 19(2): 95-110,
512 [https://doi.org/10.1016/0165-232X\(91\)90001-W](https://doi.org/10.1016/0165-232X(91)90001-W), 1991.

513 Hjort, J., Karjalainen, O., Aalto, J., Westermann, S., Romanovsky, V. E., Nelson, F. E.,
514 Etzelmüller, B., and Luoto, M.: Degrading permafrost puts Arctic infrastructure at risk by
515 mid-century. *Nat. Commun.*, 9, 5147, <https://doi.org/10.1038/s41467-018-07557-4>, 2018.

516 Hu, G., Zhao, L., Li, R., Wu, T., Pang, Q., Wu, X., Qiao, Y., and Shi J.: Characteristics of
517 hydro-thermal transfer during freezing and thawing period in permafrost regions, *Soils*,
518 46(2): 355-360, 2014. (in Chinese with English abstract)

519 Indoria, A. K., Sharma, K. L., Reddy, K. S.: Hydraulic properties of soil under warming

520 climate, in: *Climate Change and Soil Interactions*, edited by: Edited by: Prasad M. N. V.
521 and Pietrzykowski M., Elsevier, 473-508,
522 <https://doi.org/10.1016/B978-0-12-818032-7.00018-7>, 2020.

523 Kane, D. L., Hinzman, L. D., and Zarling J. P: Thermal response of the active layer to
524 climatic warming in a permafrost environment, *Cold Reg. Sci. Technol.*, 19(2): 111-122.,
525 [https://doi.org/10.1016/0165-232X\(91\)90002-X](https://doi.org/10.1016/0165-232X(91)90002-X), 1991.

526 Li, S. D.: Permafrost found on Mahan Mountains near Lanzhou (in Chinese). *J. Glaciol.*
527 *Geocryol.*, 8(4), 409–410, 1986.

528 Li, X., Che, T., Li, X., Wang, L., Duan, A., Shanguan, D., Pan, X., Fang, M., and Bao, Q.:
529 CASEarth Poles: Big Data for the Three Poles, *Bull. Am. Meteorol. Soc.*, 101(9), E1475–
530 E1491, <https://doi.org/10.1175/BAMS-D-19-0280.1>, 2020.

531 Li, X., Cheng, G., Wang, L., Wang, J., Ran, Y., Che, T., Li, G., He, H., Zhang, Q., Jiang, X.,
532 Zou, Z., and Zhao, G.: Boosting geoscience data sharing in China, *Nat. Geosci.*, 14, 541–
533 542, <https://doi.org/10.1038/s41561-021-00808-y>, 2021a.

534 Li, X., Wu, T., Wu, X., Chen, J., Zhu, X., Hu, G., Li, R., Qiao, Y., Yang, C., Hao, J. and Ni, J.:
535 Assessing the simulated soil hydrothermal regime of the active layer from the Noah-MP
536 land surface model (v1. 1) in the permafrost regions of the Qinghai–Tibet Plateau, *Geosci.*
537 *Model Dev.*, 14(3): 1753-1771, <https://doi.org/10.5194/gmd-14-1753-2021>, 2021b.

538 Li, Z., Li, S., and Wang, Yi.: Regional features of permafrost in Mahan Mountain and their
539 relationship to the environment (in Chinese). *J. Glaciol. Geocryol.*, 15(1), 83-89,
540 <https://doi.org/10.12785/amis/070422>, 1993.

541 Liu, W., Xie, C., Zhao, L., Wu, T., Li, R., Wang, W., and Qiao, Y.: Simulating the active layer
542 depth and analyzing its influence factors in permafrost of the Mahan Mountain, Lanzhou
543 (in Chinese). *J. Glaciol. Geocryol.*, 37(6), 1443-1452,
544 <https://doi.org/10.7522/j.isnn.1000-0240.2015.0160>, 2015.

545 Mathias, S. A., Skaggs, T. H., Quinn, S. A., Egan, S. N. C., Finch, L. E., and Oldham, C. D.:
546 A soil moisture accounting-procedure with a Richards' equation-based soil
547 texture-dependent parameterization, *Water Resour. Res.*, 51(1): 506-523,
548 <https://doi.org/10.1002/2014WR016144>, 2015.

549 Mu, C., Wu, X., Zhao, Q., Smoak, J. M., Yang, Y., Hu, L., and Zhang, T.: Relict mountain

550 permafrost area (LoessPlateau, China) exhibits high ecosystem respiration rates and
551 accelerating rates in response to warming. *J. Geophys. Res.: Biogeosci.*, 122, 2580-2592.
552 <https://doi.org/10.1002/2017JG004060>, 2017.

553 Nauta, A. L., Heijmans, M. M. P. D., Blok, D., Limpens, J., Elberling, B., Gallagher, A., Li,
554 B., Petrov, R.E., Maximov, T.C., van Huissteden, J., and Berendse, F.: Permafrost collapse
555 after shrub removal shifts tundra ecosystem to a methane source. *Nat. Clim. Chang.*, 5,
556 67-70. <https://doi.org/10.1038/nclimate2446>, 2015.

557 Nelson, F. E., Anisimov, O.A., and Shiklomanov, N. I.: Subsidence risk from thawing
558 permafrost - The threat to man-made structures across regions in the far north can be
559 monitored, *Nature*, 410(6831): 889-890, <https://doi.org/10.1038/35073746>, 2001.

560 Nelson, F. E., Shiklomanov, N. I., Hinkel, K. M., Christiansen, H H.: The Circumpolar active
561 layer monitoring (CALM) Workshop and THE CALM II Program. *Polar Geogr.*, 28(4):
562 253-266, <https://doi.org/10.1080/789610205>, 2004.

563 Nitu R, Roulet Y A, Wolff M, et al. WMO Solid Precipitation Intercomparison Experiment
564 (SPICE) (2012-2015). Instruments and Observing Methods Rep. 131, World
565 Meteorological Organization, 2018, 21445 pp.,
566 https://library.wmo.int/doc_num.php?explnum_id55686.

567 Obu, J., Westermann, S., Bartsch, A., Berdnikov, N., Christiansen, H. H., Dashtseren, A.,
568 Delaloye, R., Elberling, B., Etzelmüller, B., Kholodov, A., Khomutov, A., Kääb, A.,
569 Leibman, M. O., Lewkowicz, A. G., Panda, S. K., Romanovsky, V., Way, R. G.,
570 Westergaard-Nielsen, A., Wu, T., Yamkhin, J., and Zou, D.: Northern Hemisphere
571 permafrost map based on TTOP modelling for 2000–2016 at 1 km² scale, *Earth-Sci. Rev.*,
572 193, 299–316, <https://doi.org/10.1016/j.earscirev.2019.04.023>, 2019.

573 Park, H., Kim, Y., and Kimball, J. S.: Widespread permafrost vulnerability and soil active
574 layer increases over the high northern latitudes inferred from satellite remote sensing and
575 process model assessments, *Remote Sens. Environ.*, 175, 349–358,
576 <https://doi.org/10.1016/j.rse.2015.12.046>, 2016.

577 Park, H., Launiainen, S., Konstantinov, P. Y., Iijima, Y., and Fedorov, A. N.: Modeling the
578 effect of moss cover on soil temperature and carbon fluxes at a tundra site in northeastern
579 Siberia. *J. Geophys. Res.: Biogeosci.*, 123(9): 3028-3044, <https://doi.org/>

580 [10.1029/2018JG004491](https://doi.org/10.1029/2018JG004491), 2018.

581 Romanovsky, V. E, Drozdov, D. S, Oberman, N. G., Malkova, G. V., Kholodov, A. L.,
582 Marchenko, S. S., Moskalenko, N. G., Sergeev, D. O., Ukraintseva, N. G., Abramov, A. A.,
583 Gilichinsky., D. A. and Vasiliev., A. A.: Thermal state of permafrost in Russia, *Permafrost
584 Periglac. Process.*, 21(2), 136-155, <https://doi.org/10.1002/ppp.683>, 2010.

585 Romanovsky, V. E., and Osterkamp, T. E.: Interannual variations of the thermal regime of the
586 active layer and near - surface permafrost in northern Alaska. *Permafrost Periglac. Process.*,
587 6(4): 313-335, <https://doi.org/10.1002/ppp.3430060404>, 1995.

588 Shogren, A. J., Zarnetske, J. P., Abbott, B. W., Bratsman, S., Brown, B., Carey, M. P.,
589 Fulweber, R., Greaves, H. E., Haines, E., Iannucci, F., Koch, J. C., Medvedeff, A.,
590 O'Donnell, J. A., Patch, L., Poulin, B. A., Williamson, T. J., and Bowden, W. B.: Multi-year,
591 spatially extensive, watershed-scale synoptic stream chemistry and water quality conditions
592 for six permafrost-underlain Arctic watersheds, *Earth Syst. Sci. Data*, 14, 95-116,
593 <https://doi.org/10.5194/essd-14-95-2022>, 2022.

594 Smith, S. L., O'Neill, H. B., Isaksen, K., Noetzli, J., and Romanovsky, V. E.: The changing
595 thermal state of permafrost. *Nat Rev Earth Environ.*, 3(1): 10–23.
596 <https://doi.org/10.1038/s43017-021-00240-1>, 2022.

597 Sun, G. J., and Zhao, S. L.: The study on vegetation of Mahan Mountain in Gansu (in
598 Chinese). *Acta Bot. Boreal.-Occid. Sin.* 15(5), 115-120, 1995.

599 Van Everdingen, R. O.: Multi-Language Glossary of Permafrost and Related Ground-Ice
600 Terms in Chinese, English, French, German, Icelandic, Italian, Norwegian, Polish,
601 Romanian, Russian, Spanish, and Swedish. International Permafrost Association,
602 Terminology Working Group, The Arctic Institute of North America, The University of
603 Calgary, Alberta, Canada,
604 [https://globalcryospherewatch.org/reference/glossary_docs/Glossary_of_Permafrost_and](https://globalcryospherewatch.org/reference/glossary_docs/Glossary_of_Permafrost_and_Ground-Ice_IPA_2005.pdf)
605 [Ground-Ice_IPA_2005.pdf](https://globalcryospherewatch.org/reference/glossary_docs/Glossary_of_Permafrost_and_Ground-Ice_IPA_2005.pdf), 1998.

606 Walvoord, M. A., and Kurylyk, B. L.: Hydrologic impacts of thawing permafrost-a review. 15
607 (6), [vzj2016.01.0010](https://doi.org/10.2136/vzj2016.01.0010), <https://doi.org/10.2136/vzj2016.01.0010>, 2016.

608 Wang, D., Wu, T., Zhao, L., Mu, C., Li, R., Wei, X., Hu, G., Zou, D., Zhu, X., Chen, J., Hao,
609 J., Ni, J., Li, X., Ma, W., Wen, A., Shang, C., La, Y., Ma, X., and Wu, X.: A 1 km resolution

610 soil organic carbon dataset for frozen ground in the Third Pole, *Earth Syst. Sci. Data*, 13,
611 3453-3465, <https://doi.org/10.5194/essd-13-3453-2021>, 2021.

612 Westermann, S., Langer, M., and Boike, J.: Spatial and temporal variations of summer surface
613 temperatures of high-arctic tundra on Svalbard – Implications for MODIS LST based
614 permafrost monitoring, *Remote Sens. Environ.*, 115, 908–922,
615 <https://doi.org/10.1016/j.rse.2010.11.018>, 2011.

616 Westermann, S., Langer, M., Boike, J., Heikenfeld, M., Peter, M., Etzelmuller, and B.,
617 Krinner, G.: Simulating the thermal regime and thaw processes of ice-rich permafrost
618 ground with the land-surface model CryoGrid 3, *Geosci. Model Dev.*, 9(2): 523–546.
619 <https://doi.org/10.5194/gmd-9-523-2016>, 2016.

620 Xie, C., Gough, W. A., Tam, A., Zhao, L., and Wu, T.: Characteristics and Persistence of
621 Relict High-Altitude Permafrost on Mahan Mountain, Loess Plateau, China, *Permafr.*
622 *Periglac. Process.*, 24, 200-209, <https://doi.org/10.1002/ppp.1776>, 2013.

623 Xu, X., Zhang, B., and Tian, J.: Experimental study on the precipitation-soil
624 water-groundwater transformation in loess hilly region, *Adv. Water Sci.*, 21(1): 16-22, 2010.
625 (in Chinese with English abstract)

626 Zhang, G., Ran, Y., Wan, W., Luo, W., Chen, W., Xu, F., and Li, X.: 100 years of lake
627 evolution over the Qinghai-Tibet Plateau, *Earth Syst. Sci. Data*, 13, 3951-3966,
628 <https://doi.org/10.5194/essd-13-3951-2021>, 2021.

629 Zhang, T., Heginbottom, J. A., Barry, R. G., and Brown, J.: Further Statistics on the
630 Distribution of Permafrost and Ground Ice in the Northern Hemisphere, *Polar Geogr.*, 24,
631 14–19, <https://doi.org/10.1080/10889370009377692>, 2000.

632 Zhang, Z., Wu, Q., and Xun, X., Li, Y.: Spatial distribution and changes of Xing'an permafrost
633 in China over the past three decades. *Quat. Int.*, 523:16-24,
634 <https://doi.org/10.1016/j.quaint.2019.06.007>, 2019.

635 Zhao, L., and Sheng, Y. (Eds.): *Permafrost Survey Manual*, Science Press, Beijing, China,
636 2015.

637 Zhao, L., Wu, Q. B., Marchenko, S. S., and Sharkhuu, N.: Thermal state of permafrost and
638 active layer in Central Asia during the International Polar Year. *Permafr. Periglac. Process.*,
639 21(2), 198-207, <https://doi.org/10.1002/ppp.688>, 2010.

640 Zhao, L., Zou, D., Hu, G., Wu, T., Du, E., Liu, G., Xiao, Y., Li, R., Pang, Q., Qiao, Y., Wu, X.,
641 Sun, Z., Xing, Z., Sheng, Y., Zhao, Y., Shi, J., Xie, C., Wang, L., Wang, C., & Cheng, G.: A
642 synthesis dataset of permafrost thermal state for the Qinghai-Xizang (Tibet) Plateau, China.
643 Earth Syst. Sci. Data, 13, 4207–4218. <https://10.5194/essd-13-4207-2021>, 2021a
644 Zhao, Y., Chen, R., Han, C., Wang, L., Guo, S., Liu J.: Correcting precipitation measurements
645 made with Geonor T-200B weighing gauges near the August-one ice cap in the Qilian
646 Mountains, Northwest China, Journal of Hydrometeorology, 22(8): 1973-1985.
647 <https://doi.org/10.1175/JHM-D-20-0271.1>, 2021b.
648 Zhu, X., Wu, T., Li, R., Xie, C., Hu, G., Qin, Y., Wang, W., Hao, J., Yang, S., Ni, J., and Yang,
649 C.: Impacts of summer extreme precipitation events on the hydrothermal dynamics of the
650 active layer in the Tanggula permafrost region on the Qinghai-Tibetan Plateau, J. Geophys.
651 Res. Atmos., 122: 11549-11567. <https://doi.org/10.1002/2017JD026736>, 2017.
652 Zou, D., Zhao, L., Sheng, Y., Chen, J., Hu, G., Wu, T., Wu, J., Xie, C., Wu, X., Pang, Q.,
653 Wang, W., Du, E., Li, W., Liu, G., Li, J., Qin, Y., Qiao, Y., Wang, Z., Shi, J., and Cheng, G.:
654 A new map of permafrost distribution on the Tibetan Plateau, Cryosphere, 11, 2527-2542,
655 <https://doi.org/10.5194/tc-11-2527-2017>, 2017.